

Mechanical properties and deformation mechanisms of a novel austenite-martensite dual phase steel

S.S. Xu ^a, J.P. Li ^a, Y. Cui ^a, Y. Zhang ^a, L.X. Sun ^a, J. Li ^b, J.H. Luan ^c, Z.B. Jiao ^d, X.-L. Wang ^e, C.T. Liu ^c, Z.W. Zhang ^{a,*}

^a Key Laboratory of Superlight Materials and Surface Technology, Ministry of Education, College of Materials Science and Chemical Engineering, Harbin Engineering University, Harbin, 150001, China

^b Key Laboratory of Neutron Physics and Institute of Nuclear Physics and Chemistry, China Academy of Engineering Physics (CAEP), Mianyang, 621999, China

^c Department of Materials Science Engineering, College of Science and Engineering, City University of Hong Kong, Hong Kong, China

^d Department of Mechanical Engineering, The Hong Kong Polytechnic University, Hong Kong, China

^e Department of Physics, City University of Hong Kong, Hong Kong, China

ABSTRACT

A novel austenite-martensite dual-phase steel with a ductility of ~30% and tensile strength over 1.4 GPa was developed. The hard martensite in the dual phase steel was strengthened through precipitation strengthening by Cu/NiAl precipitates, forming the maraging phase. The deformation mechanisms of the steel were investigated using in situ neutron diffraction and transmission electron microscopy (TEM). The results indicate that the maraging phase constrains the deformation of soft austenite, forming a strong skeleton frame with the soft austenite involved in the frame. The yield strength was controlled by the deformation of hard maraging phase, leading to the high strength of the steel. The plasticity of the maraging phase was improved through the synchronously deformation and rotation of martensite grains along with the frame-structure effect. During deformation of the maraging phase, the transfer of the dynamic stress and strain from

the hard phase to a soft one compels the cooperative deformation of the soft phase together with the hard phase. This deformation contributes further to the ductility through the transformation-induced plasticity (TRIP) effects of the soft austenite. Furthermore, the cooperative deformation and the dynamic stress/strain partitions can effectively suppress the strain localization at the phase interface, retarding the crack initiation.

1. Introduction

Advanced high-performance structural materials with both gigapascal strength and large ductility are highly necessary for reducing weight and improving energy efficiency. Dual-phase (DP) steels consisting of soft and hard phases can provide a combination of good strength, ductility and a high work-hardening rate, alleviating the strength-ductility trade-off (Tasan et al., 2015). In DP steels, the high ductility originates from the better strain hardening behavior of the soft phase through the pronounced dislocation activities (Kad-khodapour et al., 2011b), the formation of twinning (He et al., 2016), and strain partitioning or strain-induced phase transformation (Ennis et al., 2017; Wang et al., 2015). However, the soft phase controls the yielding of DP steels and gives rise to a low yield strength. The hard phase can provide a limited increment in the strength via interface hardening by resisting the dislocation slip in the soft phase (Ghassemi-Armaki et al., 2014).

The transformation-induced plasticity (TRIP) effect, as one of the most effective approaches to increase the work-hardening rate together with ductility and strength (Jacques et al., 1998, 1999), has been observed in the TRIP steel (Fischer et al., 2000; Kim et al., 2003; Petrov et al., 2007; Saleh and Priestner, 2001), medium-manganese steel (Cao et al., 2011; Gräßel et al., 2000), quenching and partitioning steel (Zhang et al., 2011) and TRIP-maraging steel (Raabe et al., 2009).

The TRIP effect is based on the deformation-induced transformation of the metastable austenite to martensite, achieving a high work-hardening rate to reach a high uniform elongation. In the TRIP-maraging steel consisting of uniformly distributed austenite and martensite, the deformation and phase transformation of the metastable austenite are usually observed in small strains, and only a small number of martensitic grains with preferred orientations can synergistically deform (Wang et al., 2014, 2015). Under this condition, strain localizations are apt to form at the interface between austenite and undeformed martensite. Moreover, when the martensite phase is much harder than the soft phase to further improve the strength, microcracks will be inevitably nucleated at the interface between two phase (Fujita et al., 2018; Kim et al., 2017), resulting in the ductility reduction.

Sustained efforts have been paid to overcome the shortcomings of dual phase (DP) steels. The microstructural features such as hard phase volume fraction and properties are usually adjusted to improve properties (Lai et al., 2016). Micromechanisms developed for DP steels are based on dispersion hardening models that deal mainly with the work-hardening rate of the soft phase (Szewczyk and Gurland, 1982). Various properties of the hard phase caused by thermomechanical treatment or precipitation/dispersion hardening can effectively improve either the strength or ductility but it is difficult to improve both of these properties (Ismail et al., 2019; Pierman et al., 2014). Another example is the aging embrittlement in the ferrite/austenite DP steel where spinodal decomposition in the ferrite enhanced the hard ferrite phase, leading to embrittlement (Weng et al., 2004). The strength can be significantly affected by the stress borne by the hard phase. However, the hard constituent is usually subject to incompatibility stresses that eventually lead to fracture due to the soft/hard phase interfacial decohesion (Ahmad et al., 2012; Kadkhodapour et al., 2011a; Raabe et al., 2009), or hard phase cracking (Matsuno et al., 2015).

In this study, an austenite-martensite dual phase steel was developed through a careful alloy design effort. The microstructure of the DP steel was obtained by high strength maraging phase, which is strengthened by nanoscale Cu and NiAl precipitates. The distributions of nanoscale precipitates in both maraging phase and austenite were systematically characterized by atom probe tomography (APT). The deformation mechanisms were investigated using in-situ neutron diffraction, TEM and electron backscattered diffraction (EBSD) techniques. The effects of the deformation mechanisms on the mechanical properties are also carefully addressed and discussed.

2. Experimental

2.1. Material preparation

The steel which has a chemical composition of Fe–9Mn–4Ni–1Al–2.5Cu–1.5Mo–1.5W–0.1Ti–0.05Nb–0.5Si–0.08C was prepared by arc-melting purity metals. The ingots were re-melted five times to ensure chemical homogeneity and then drop-cast into rods of 20 mm in diameter in a water-cooled copper mold. The as-cast ingots were hot-rolled at 900 °C from 20 to 2 mm thickness and solid-solution treated for 1 h at 900 °C followed by water quenching (Labeled as SS). The SS specimen was then aged at 500 °C in air for 5 min (AG5min), 15 min (AG15min), 0.5 h (AG0.5h), 45 min (AG45min), 1 h (AG1h), 2 h (AG2h), 5 h (AG5h) and 50 h (AG50h).

2.2. Characterizations of mechanical properties and microstructure

Hardness measurements were conducted using a Vickers tester with the loads of 500 g (hard phase) and 100 g (soft phase) for 15 s. For each value, at least ten indentations were measured to obtain an average value. Tensile tests along the rolling direction of the samples were conducted using an Instron 5565 testing machine at a strain rate of 10^{-3} s^{-1} . Three specimens were tested in

each condition and average values were reported. The gauge length, width and thickness of the tensile specimens were 12.5, 4 and 1 mm, respectively. A contacting Instron extensometer was used to measure the strain within the sample gauge upon loading. The yield strength was determined using the 0.2% offset plastic strain method.

Electron backscattering diffraction (EBSD), X-ray diffraction (XRD) and transmission electron microscopy (TEM) were performed to characterize the phase components and microstructures of the samples. The EBSD measurements were carried out using a Hitachi S3400 scanning electron microscope (SEM) equipped with HKL Channel 5 software. The phase compositions were determined using an energy dispersive X-ray spectrometer (EDS) attached to the SEM. At least six points in both the austenite and martensite phases were measured to obtain an average value of each element before and after aging. Austenite volume fraction in both the SS and AG0.5h samples before and after the tensile tests were measured by XRD with Cu-K α radiation using a D/max-2550 X-ray diffractometer. Austenite peaks of the (200), (220), (311) planes and martensite peaks of the (220), (211) planes were selected for the calculation of the volume fraction of austenite according to Eq. (1) and the volume fraction of austenite is obtained as the average of V_i (Wang et al., 2010).

$$V_i = \frac{1}{1 + G(I_\alpha/I_\gamma)} \quad (1)$$

where V_i is the volume fraction of austenite for each peak, I_α and I_γ are the integrated intensities of the martensite and austenite peaks, respectively, and G is the ratio of the intensity factor corresponding to the austenite crystal plane (hkl) and the martensite crystal plane (hkl), and h, k, l are the corresponding crystal indices. G -value for each peak was used as follow, 2.5 for $I_{\alpha(200)}/I_{\gamma(200)}$,

1.38 for $I_{\alpha(200)}/I_{\gamma(220)}$, 2.02 for $I_{\alpha(200)}/I_{\gamma(311)}$, 1.19 for $I_{\alpha(211)}/I_{\gamma(200)}$, 0.06 for $I_{\alpha(211)}/I_{\gamma(220)}$, 0.96 for $I_{\alpha(211)}/I_{\gamma(311)}$ (Wang et al., 2010).

Nanoscale precipitates were characterized using atom probe tomography (APT). The needle-shaped specimens for APT were fabricated by lift-outs and were annular milled in an FEI Scios focused ion beam/scanning electron microscope (FIB/SEM) (Miller et al., 2005). The APT characterizations were performed in a local electrode atom probe (CAMEACA LEAP 5000 R). The specimens were analyzed at 50 K in the voltage mode with a pulse repetition rate of 200 kHz, a pulse fraction of 20%, and an evaporation detection rate of 0.5% atom per pulse. This high pulse repetition rate significantly reduces the possibility of preferential evaporation of the low evaporation field solutes, e.g. copper (Miller et al., 2006). Imago Visualization and Analysis Software (IVAS) version 3.8 was used for creating the 3D reconstructions and data analysis. Cu-enriched precipitates were identified using the maximum separation method (Hyde et al., 2001). The 8% Cu and 15% (Ni+Al) concentration isosurfaces were used to visualize the NiAl and Cu nanoprecipitates, respectively.

2.3. In-situ neutron diffraction experiments

The in-situ neutron diffraction experiments were performed on the Residual Stress Neutron Diffractometer (RSND) at China Academy of Engineering Physics (CAEP) in Mianyang. The neutron flux on the sample position is 4.7×10^6 n/cm²/s at the wavelength λ 0.158 nm with the reactor power of 20 MW. The detailed equipment and related parameters can be found in Ref. (Li et al., 2015). The tensile specimens were cut from the sheets along the rolling direction by an electronic discharge machine. The sample dimensions and position for the measurements are shown in Fig. 1. The macroscopic strain was determined concurrently using a tensile tester with an extensometer that spanned the irradiated region at room temperature with a strain rate of 6.7×10^{-3}

⁴ s⁻¹. The diffraction volume was centered in the middle of the gauge length. Experiments were carried out with controlled strain, and the sample for each loading level was deformed to the desired strain and held for 30 s to allow for stress relaxation prior to beginning the data collection. The neutron diffraction profiles were collected during tensile loading and analyzed by fitting a single Gaussian distribution to each reflection in order to determine the position of each peak. The {hkl} lattice strain, ϵ_{hkl} , was determined from the average interplanar lattice spacing d_{hkl} for an hkl grain family of the martensite or austenite phase. The shift in the Bragg reflections from the change in lattice plane spacing under the influence of a stress field is determined to obtain the lattice strains in the grains with reference to the measured stress-free lattice space d_{hkl}^0 (Dye et al., 2001; Holden et al., 1997; Wang, 2006). The lattice strain is calculated using the following equation (Shen et al., 2013):

$$\epsilon_{hkl} = (d_{hkl} - d_{hkl}^0) / d_{hkl}^0 \quad (2)$$

where d_{hkl} is the interplanar spacing under an applied load and d_{hkl}^0 is the reference spacing measured at zero load at the start of the test. We note that all of the BCC reflections were associated with the entire martensite phase in the neutron diffraction. Therefore, two phases were considered in the current analysis of the neutron diffraction data: (I) α' -martensite and (II) γ -austenite. Once dislocation slip has been initiated in certain grains, further deformation is accommodated plastically with little increase in the load supported by the grains. At this point, a greater proportion of the applied load will be partitioned to those grains that have not yet yield. This results in a departure from linearity of the response of the lattice strain to the applied load. Thus, based on the departure, the deformation mechanisms can be investigated (Dye et al., 2001; Holden et al., 1997; Wang, 2006). The development of intergranular microstress is dependent upon the elastic and plastic anisotropy intrinsic to the material. In this study, the response of lattice strains to load stress

of the crystal planes of {110}, {200} and {211} for BCC martensite and {111}, {200}, {220}, {311} for FCC austenite were determined.

3. Results

3.1. Mechanical properties

Room-temperature tensile tests are performed to investigate the mechanical properties of the austenite-martensite dual phase steels, and the engineering stress-strain curves of the solid-solution treated (SS) and aged (AG0.5h) DP samples are shown in Fig. 2a. The SS steel exhibits a low yield strength of 619 ± 12 MPa and an ultimate tensile strength of 1149 ± 24 MPa with a uniform elongation of 9.7%. After aging for 0.5 h at 500 °C, the yield strength increases significantly to as high as 1269 ± 25 MPa, together with a double increment in the uniform tensile elongation, from 9.7% to 19.2%. Notably, a simple aging treatment leads to a simultaneous increase in the strength and ductility, evading the strength-ductility trade-off dilemma. Fig. 2b shows the tensile properties of the dual-phase steel with comparison to other high-performance materials, including conventional dual-phase steels (Ahmad et al., 2000; Azizi-Alizamini et al., 2011; Bergström et al., 2010; Calcagnotto et al., 2011; Kim et al., 2003; Li et al., 2017; Saleh and Priestner, 2001; Szewczyk and Gurland, 1982; Torabian et al., 2017; Zhang et al., 2014), martensitic steels (Arlazarov et al., 2013; Jiang et al., 2017; Sun et al., 2018), precipitation-strengthened steels (Jiao et al., 2015; Kapoor et al., 2014; Xu et al., 2019), TRIP steels (Jacques et al., 1998; Zhang et al., 2006; Zhao et al., 2012), maraging-TRIP steels (Raabe et al., 2009; Wang et al., 2014, 2015), quenching and partitioning (QP) steels (Zhang et al., 2011), 316L austenite stainless steels (Yan et al., 2012), nanostructured lamella Ti (Wu et al., 2015), nanostructured Mo alloy (Liu et al., 2013) and Ti6Al4V (Kim et al., 2015). Our dual phase steel shows a large ductility which is three times

higher than that of the conventional martensitic steels with the same strength level. Moreover, the strength is much greater than that of the conventional dual-phase steels and TRIP steels.

3.2. Microstructure characterizations

To attain precise information of microstructures, the microstructure and orientation mappings with low ($2-15^\circ$) and high angle ($15-180^\circ$) grain boundaries (GBs) of SS and AG0.5h DP steels obtained by EBSD are shown in Fig. 3. Both SS and AG0.5h steels consist of two phases: the lath α_0 -martensite with the body-centered cubic (BCC) structure (red color) and the γ -austenite with a face-centered cubic (FCC) structure (blue color) as shown in Fig. 3a and b. The neighboring martensite laths are separated by low-angle grain boundaries (LAGB) in Fig. 3c and d. The γ -austenite with an elongated structure paralleling to the rolling direction has the lath martensite. The compositions of the austenite and martensite phase in the SS and AG0.5h steel are listed in Table 1. The statistical distributions of the grain size are shown in Fig. 4. Austenite contains a higher concentration of Mn, Cu and Ni as compared in martensite due to their higher solubility. The concentration in both austenite and martensite does not change apparently before and after aging treatment. The grain sizes of the austenite and martensite in both SS and AG0.5h steels are similar with a mean size of $\sim 1 \mu\text{m}$.

However, the volume fraction of the austenite in the DP steel increases obviously after aging as shown in Fig. 3. In order to attain precise information about the change in the volume fraction of austenite, the volume fraction of austenite in SS and AG0.5h steels before and after the tensile tests (SS-AT and AG0.5h-AT) was measured by X-ray Diffraction (XRD) and is shown in Fig. 5. The volume fraction of the austenite increases from $\sim 27.8\%$ to 34.5% after aging for 0.5 h at 500°C , indicating that aging introduces some reversed austenites. But the volume fraction of the austenite in the SS and AG0.5h steels after a uniform deformation decreased by 17.6% and 13.4% ,

respectively, indicating the occurrence of transformation-induced plasticity (TRIP) from the austenite to martensite during the deformation. Actually, this change is comparable with the results from a similar TRIP-maraging steel (Wang et al., 2014).

3.3. APT characterization of nanoscale precipitation

The evolution of the microhardness upon aging is shown in Fig. 6a for both the martensite and austenite in the dual-phase steel. The hardness of the austenite shows no appreciable change upon aging and remains almost a constant at ~200 HV. However, the aging treatment results in a high age hardening in the martensite phase. Under the solid solution condition, the martensite phase has a hardness of ~375 HV. Subsequently, its hardness gradually increases with the aging time and reaches a peak value of ~530 HV after aging for 0.5 h at 500 °C. Prolonging aging leads to a gradual decline, owing to the over-aging effect. The distributions of the solute elements in both austenite and martensite in AG0.5h steels were characterized carefully by APT and are shown in Fig. 6b and c, respectively. In the austenite phase, the Cu, Ni, Al and Mn solute elements are distributed uniformly in the supersaturated solid solution (Fig. 6b) and no precipitates except minor carbide are detected. The atomic ratio of Ti: Mo: C in the carbide as shown in Fig. 6d is approximately 1:1:2, corresponding to (Ti, Mo)C-type carbides. On the other hand, a large amount of nanoscale precipitates can be identified clearly in the martensite, forming the maraging phase (Decker and Floreen, 1988) (Fig. 6c). These nanoscale precipitates are either enriched with Cu and Ni, forming Cu-rich precipitates, or they are enriched with Ni, Al and Mn and form NiAl rich precipitates. The average radius of the Cu-rich and NiAl-rich nanoprecipitates are 1.7 ± 0.6 and 1.8 ± 0.7 nm, respectively. Their number densities are 9.28×10^{23} and $1.12 \times 10^{24} \text{ m}^{-3}$, respectively. The proximity histograms of the Cu and NiAl nanoprecipitates are displayed in Fig. 6e and f. For the Cu-rich precipitates, Cu is enriched (54.4 ± 3.2 at.%) together with Ni in the particle center,

whereas some Ni, Al and Mn are detected at the precipitate-matrix interface. The NiAl precipitates are enriched in Ni (32.4 ± 3.9 at.%), Al (23.4 ± 3.9 at.%) and Mn (22.6 ± 4.5 at.%) together with some Cu (10.0 ± 1.9 at.%).

3.4. In situ neutron diffraction

Deformation mechanisms of the dual-phase steel before and after aging were investigated using in situ neutron diffraction as shown in Fig. 7 and Fig. 8. It can be seen from Fig. 7 that at the yielding point of SS steel, the lattice strain of $\{211\}$ plane in α' -martensite loses the linear relationship between the lattice strains and the applied stress. This indicates that slip has been initiated in these grains oriented with $\{211\}$ plane perpendicular to the loading direction. These grains in α' -martensite are responsible for the yielding behavior of this steel even though all of the $\{111\}$, $\{200\}$, $\{220\}$ and $\{220\}$ planes in austenite deform before yielding. Beyond the yielding point, only the $\{211\}$ plane in α' -martensite deform continuously while the other two planes of $\{110\}$, $\{200\}$ in martensite keep elastic deformation till to fracture, leading to a big gap among the critical yielding stresses for various crystal planes of the martensite. Moreover, the responses of lattice strain for the $\{111\}$ and $\{200\}$ planes of γ -austenite beyond yielding show an obvious increment with the applied stress increasing, indicating that the $\{111\}$ and $\{200\}$ planes in the austenite are subject to large stress. In Fig. 7b, the SS steel has a gradual decrease in the strain hardening rate during the whole uniform deformation (stage II), which is similar with the reported austenite-martensite dual phase steels (Wang et al., 2015).

After aging, the martensite was significantly strengthened due to the precipitation of the nanoscale Cu/NiAl precipitates, forming the maraging phase. With the formation of high strength maraging phase, the deformation mechanisms are quite different from the SS steel. The response of the lattice strain to the applied stress along the tensile direction (i.e., loading direction) for the

AG0.5h steel can be divided into three stages (Fig. 8a). Stage I corresponds to the elastic deformation regime ($\sigma < 1269$ MPa) before yielding, stage II corresponds to the early uniform deformation regime ($1269 \text{ MPa} < \sigma < 1360$ MPa), and stage III corresponds to the late uniform deformation regime ($\sigma > 1360$ MPa).

Prior to the macro-yielding of the AG0.5h Steel (Stage I in Fig. 8a), the lattice strains for all of the lattice planes of the precipitate-strengthened martensite including $\{110\}$, $\{200\}$ and $\{211\}$ evolved linearly with the applied stress, indicating that the plastic deformation for all of the lattice planes of the martensite does not occur in this stage. While the linear relationship between the lattice strains and the applied stress for the lattice planes of $\{111\}$, $\{200\}$ and $\{220\}$ in the soft γ -austenite changes slightly when the applied stress is greater than ~ 550 MPa, indicating that the plastic deformation occurred in the soft γ -austenite in this stage. However, this plastic deformation was constrained by the precipitate-strengthened martensite and no macroplastic deformation can be detected. When the applied stress exceeds 1269 MPa, the macroplastic deformation occurs, corresponding to the yielding of the dual-phase steel (Fig. 2a). After yielding, the lattice strain of the $\{211\}$ plane in the martensite drops, while lattice strain of the $\{200\}$ plane increases, indicating that the slip of dislocation starts in the grains with $\{211\}$ plane perpendicular to loading direction. Beyond yielding in stage II of the AG0.5h steel, further deformation is accommodated plastically with little increase in the load supported by the $\{211\}$ grains of the martensite. Meanwhile, a greater proportion of the applied load is partitioned to those grains with $\{200\}$ plane perpendicular to loading direction, corresponding to the increase in the lattice strain of the $\{200\}$ plane. These are consistent with the previous results in the pure ferrite with BCC structure (Dye et al., 2001). Above ~ 1360 MPa, the $\{211\}$ and $\{200\}$ reflections of the martensite disappear while the intensity

of the $\{110\}$ component is enhanced (Fig. 9), indicating that the $\{211\}$ and $\{200\}$ planes rotate out toward $\{110\}$ during the deformation.

As for the austenite in the AG0.5h steel, the lattice strains for all of the crystal planes remain unchanged for the applied stress in the 1269-1360 MPa range. Both the peak intensities and full-width half-maxima (FWHM) of the various crystal planes in the austenite are also unchanged (Fig. 8b and c). These results demonstrate that no phase transformation occurs for austenite during the deformation in this stage because most of the applied stresses are borne by the precipitate-strengthened martensite.

When the applied stress is greater than ~ 1360 MPa (Stage III in Fig. 8a), the grains in the precipitate-strengthened martensite with $\{110\}$ plane perpendicular to loading direction starts to deform, corresponding to the decrease in the lattice strain of the $\{110\}$ plane. Meanwhile, the peak intensities of the $\{211\}$, $\{200\}$, $\{220\}$ and $\{311\}$ planes of the austenite phase drop sharply (Fig. 8b). This is consistent with the reduction in the volume fraction of the austenite during the deformation (Fig. 5), indicating the occurrence of a phase transformation from the austenite to martensite during the deformation. The activation of the $\{110\}$ slip system is beneficial to the transfer of the stress and strain from the martensite to austenite due to the optimal crystallization relationship. At the same time, the FWHM of $\{200\}\gamma$ and $\{111\}\gamma$ changes (Fig. 8c), indicating the deformation of these two crystal planes. Fig. 8e shows a low kernel average misorientation (KAM) value of the austenite after the tensile deformation, confirming that a reduction in the volume fraction of the austenite is induced by the phase transformation from the austenite to martensite. Meanwhile, a small amount of the austenite deforms as indicated by the change of a kernel average misorientation.

4. Discussion

4.1. Nanoscale precipitation in martensite

Upon aging, the mechanical properties can be enhanced significantly while the matrix microstructure has no apparent changes, indicating that both the increment in strength and ductility can be mainly attributed to the precipitation strengthening of the martensite. It is clear that a high number density of ultrafine Cu and NiAl nanoprecipitates are precipitated out only in the martensite after the aging treatment (Fig. 6), leading to the pronounced aging-hardening. A typical Cu-rich and NiAl-rich coprecipitates are as shown in Fig. 10. The threshold values of Cu (8 at.%) and NiAl (15 at.%) isosurfaces were selected to visualize the precipitate. The precipitation characteristics of Cu/NiAl coprecipitates in martensite, such as size, number density, composition and morphology, are similar to that in the similar nanoprecipitate-strengthened ferritic steels (Kapoor et al., 2014; Wen et al., 2013), indicating that the nanoscale precipitation can be successfully controlled in martensite in the austenite-martensite dual phase steels. The strengthening mechanisms of Cu/NiAl co-precipitates in the similar nanoprecipitate-strengthened ferritic steels are applicative to the martensite in the dual-phase steel (Jiao et al., 2017; Xu et al., 2017, 2019). Therefore, the martensite is clearly strengthened by the large amount of coprecipitates after the aging treatment for 0.5 h, forming the maraging phase, while the strength of austenite remains unchanged upon the aging treatment.

4.2. Deformation mechanisms and its effects on the mechanical properties

The in-situ neutron diffraction results (Figs. 7 and 8) indicate that the plastic-deformation mechanisms of the dual phase steel changed after aging for 0.5 h. The precipitate-strengthened martensite forms a strong skeleton frame with the soft austenite wrapped in the frame, forming the unique dual-phase microstructure in the AG0.5h steel. The significant simultaneous improvement

in both ductility and strength can be correlated to the formation of the maraging phase and the frame structure in the dual-phase steel. With the unique dual-phase structure, the maraging phase constrains the plastic deformation of the soft austenite in AG0.5h DP steel during elastic deformations, and meanwhile controls the yielding behavior. Similar phenomena are also observed for the SS steel due to its similar phase components and microstructure. The yielding of the {211} plane in the martensite also controls the macro yielding point. However, the yield strength is not high due to the low strength of the martensite without the nanoprecipitates, as shown in Figs. 2a and 7a.

With the formation of the maraging phase in the AG0.5h steel, the gap between the critical yielding stresses for various crystal planes in martensite is narrowed during the early uniform deformation (stage II in Fig. 8a), leading to an almost simultaneous deformation and rotation of the {211} and {200} planes. While no deformation and phase transformation in soft austenite occur in this stage. Therefore, the deformation and rotation on the {211} and {200} planes of the enhanced martensite together with the continuous transfer of the stresses among the different crystal planes in the martensite engage the deformation capability of the maraging phase, contributing to the large initial uniform macroplastic deformation. By contrast, without the precipitation-strengthening of the martensite (SS steel), there is a large gap between the critical yielding stresses for the various crystal plane of the martensite and only the {211} plane deforms after yielding till fracture (Fig. 7a).

The rotation of the {211} and {200} planes toward {110} during the deformation promotes the formation of the crystallographic orientation relationship of $(011)\alpha'// (1-1-1)\gamma$ between the martensite and the austenite which is beneficial for the activation of the slip systems of the adjacent austenite grains and finally decreasing the stress at the phase boundaries (Wang et al., 2013). The

moving dislocations in the martensite slip to the phase boundaries (Fig. 11), exhibiting a Kurdjumov-Sachs (K-S) orientation relationship with the austenite, i.e., $(111)_\gamma // (011) \alpha'$. Then, the deformation of the martensite can transfer to the austenite in the late uniform deformation (stage III). Thus, at the late stage of the uniform deformation, the transfer of the dynamic stress and strain from the hard phase to soft phase is apt to occur with the activation of the $\{110\}$ slip system, compelling the cooperative deformation of the soft phase with the hard phase. The deformation of the soft phase along with the hard phase contributes further to the ductility through the transformation-induced plasticity (TRIP) effects, forming a strain hardening plateau. The cooperative deformation and the dynamic stress and strain partition between the martensite and austenite can effectively suppress the strain localization at the phase interface, retarding the initiation of cracks. The strain hardening plateau also defers the necking point, contributing to the later uniform elongation.

5. Conclusions

In this study, we have systematically investigated the microstructural features, deformation mechanisms and mechanical properties of the newly developed austenite-martensite dual phase steel. The main conclusions can be summarized as follows.

1. A novel austenite-martensite dual-phase steel with a high ductility (~30%) and high strength (over 1.4 GPa) was developed. The unique microstructural feature with the martensite as strong skeleton filled by the soft austenite can be successfully applied to alleviate the strength-ductility trade-off.

2. Upon aging at 500 °C for 0.5 h, a high number density of Cu and NiAl nanoparticles can precipitate in the martensite phase, while no precipitates emerge in the austenite phase due to the large solubility of alloying elements in the FCC structure, confirming that the precipitation

strengthening can be successfully applied to only one phase, forming the unique maraging phase in the dual phase steel.

3. Strengthening the martensite by forming the maraging phase in the dual phase steel with the unique microstructure can effectively improve both the ductility and strength simultaneously.

4. The unique structural feature results in the transfer of the yielding behavior, from starting in the soft phase to starting in the hard one by constraining the deformation of the soft phase. The hard martensite phase enhanced by high-density Cu and NiAl nano- precipitates determines the yielding behavior, providing the high strength of the dual phase steel.

5. The large ductility can be contributed by the three aspects at various deformation stages. One is the thorough release of the plastic ability of the precipitate-strengthened martensite at the first stage of deformation due to the simultaneous activation of multiple slip systems and rotation of martensitic grains. The second is that the dynamic stress and strain between the martensite and austenite phases compel a cooperative deformation at the uniform deformation stage, forming a strain hardening plateau due to the transformation induced plasticity (TRIP) effects of the soft austenite. And the third is that the cooperative deformation and the dynamic stress/strain partitions suppress the strain localization at the phase interface, improving the later uniform elongation.

Declaration of competing interests

The authors declare that they have no known competing financial interests or personal relationships that could have appeared to influence the work reported in this paper.

CRedit authorship contribution statement

S.S. Xu: Writing - original draft, Conceptualization, Investigation, Visualization, Resources.
J.P. Li: Methodology, Investigation. Y. Cui: Visualization, Resources. Y. Zhang: Validation,

Funding acquisition. L.X. Sun: Data curation, Supervision. J. Li: Software, Formal analysis. J.H. Luan: Software, Formal analysis. Z.B. Jiao: Software, Formal analysis. X.-L. Wang: Writing - review & editing. C.T. Liu: Writing - review & editing, Funding acquisition. Z.W. Zhang: Conceptualization, Validation, Project administration, Funding acquisition.

Acknowledgments

This research project has been supported by NSFC Funding (51371062), National Key Research Program of China (2018YFE0115800), the Fundamental Research Funds for the Central Universities (HEUCFP201850), NSFHLJ (JC2017012, LH2019E030) and China Postdoctoral Science Foundation Funded Project (2019T120255, 2017M620111). The neutron diffraction work at the China Academy of Engineering Physics (CAEP) is greatly appreciated. Atom probe tomography research was conducted with the assistance of Dr. J. H. Luan and Dr. Z. B. Jiao at the Inter-University 3D Atom Probe Tomography Unit of City University of Hong Kong supported by the CityU grant 9360161 and CRF grant C1027-14E.

References

- Ahmad, E., Manzoor, T., Ali, K.L., Akhter, J.I., 2000. Effect of microvoid formation on the tensile properties of dual-phase steel. *J. Mater. Eng. Perform.* 9, 306-310. Ahmad, E., Manzoor, T., Ziai, M.M.A., Hussain, N., 2012. Effect of martensite morphology on tensile deformation of dual-phase steel. *J. Mater. Eng. Perform.* 21, 382–387.
- Arlazarov, A., Bouaziz, O., Hazotte, A., Gouné, M., Allain, S., 2013. Characterization and modeling of manganese effect on strength and strain hardening of martensitic carbon steels. *Isij Int.* 53, 1076-1080.
- Azizi-Alizamini, H., Militzer, M., Poole, W.J., 2011. formation of ultrafine grained dual phase steels through rapid heating. *ISIJ Int.* 51, 958-964.

- Bergström, Y., Granbom, Y., Sterkenburg, D., 2010. A dislocation-based theory for the deformation hardening behavior of DP steels: impact of martensite content and ferrite grain size. *J. Metall.* 2010, 1-16.
- Calcagnotto, M., Adachi, Y., Ponge, D., Raabe, D., 2011. Deformation and fracture mechanisms in fine- and ultrafine-grained ferrite/martensite dual-phase steels and the effect of aging. *Acta Mater.* 59, 658-670.
- Cao, W.Q., Wang, C., Shi, J., Wang, M.Q., Hui, W.J., Dong, H., 2011. Microstructure and mechanical properties of Fe-0.2C-5Mn steel processed by ART-annealing. *Mater. Sci. Eng.* 528, 6661-6666.
- Decker, R.F., Floreen, S., 1988. Maraging Steels-The First 30 Years. *Maraging Steels: Recent Developments and Applications*, pp. 1-38.
- Dye, D., Stone, H.J., Reed, R.C., 2001. Intergranular and interphase microstresses. *Curr. Opin. Solid St. M.* 5, 31-37.
- Ennis, B.L., Jimenez-Melero, E., Atzema, E.H., Krugla, M., Azeem, M.A., Rowley, D., Daisenberger, D., Hanlon, D.N., Lee, P.D., 2017. Metastable austenite driven work-hardening behaviour in a TRIP-assisted dual phase steel. *Int. J. Plast.* 88, 126-139.
- Fischer, F.D., Reisner, G., Werner, E., Tanaka, K., Cailletaud, G., Antretter, T., 2000. A new view on transformation induced plasticity (TRIP). *Int. J. Plast.* 16, 723-748.
- Fujita, N., Ishikawa, N., Roters, F., Tasan, C.C., Raabe, D., 2018. Experimental-numerical study on strain and stress partitioning in bainitic steels with martensite-austenite constituents. *Int. J. Plast.* 104, 39-53.
- Ghassemi-Armaki, H., Maaß, R., Bhat, S.P., Sriram, S., Greer, J.R., Kumar, K.S., 2014. Deformation response of ferrite and martensite in a dual-phase steel. *Acta Mater.* 62, 197-211.
- Grässel, O., Krüger, L., Frommeyer, G., Meyer, L.W., 2000. High strength Fe-Mn-(Al, Si) TRIP/TWIP steels development-properties-application. *Int. J. Plast.* 16, 1391-1409.
- He, B.B., Luo, H.W., Huang, M.X., 2016. Experimental investigation on a novel medium Mn steel combining transformation-induced plasticity and twinning-induced plasticity effects. *Int. J. Plast.* 78, 173-186.
- Holden, T., Holt, R., Clarke, A.P., 1997. Intergranular stresses in incoloy-800. *J. Neutron Res.* 5, 241-264.

- Hyde, J.M., Ellis, D., English, C.A., Williams, T.J., 2001. Microstructural evolution in high nickel submerged arc welds. *ASTM Inter* 1405, 262-290.
- Ismail, K., Perlade, A., Jacques, P.J., Pardoën, T., Brassart, L., 2019. Impact of second phase morphology and orientation on the plastic behavior of dual-phase steels. *Int. J. Plast.* 118, 130-146.
- Jacques, P., Delannay, F., Cornet, X., Harlet, P., Ladrière, J., 1998. Enhancement of the mechanical properties of a low-carbon, low-silicon steel by formation of a multiphased microstructure containing retained Austenite. *Metall. Mater. Trans. A* 29, 2383-2393.
- Jacques, P., Girault, E., Catlin, T., Geerlofs, N., Kop, T., van der Zwaag, S., Delannay, F., 1999. Bainite transformation of low carbon Mn-Si TRIP-assisted multiphase steels: influence of silicon content on cementite precipitation and austenite retention. *Mater. Sci. Eng.* 273-275, 475-479.
- Jiang, S., Wang, H., Wu, Y., Liu, X., Chen, H., Yao, M., Gault, B., Ponge, D., Raabe, D., Hirata, A., Chen, M., Wang, Y., Lu, Z., 2017. Ultrastrong steel via minimal lattice misfit and high-density nanoprecipitation. *Nature* 544, 460-464.
- Jiao, Z.B., Luan, J.H., Miller, M.K., Chung, Y.W., Liu, C.T., 2017. Co-precipitation of nanoscale particles in steels with ultra-high strength for a new era. *Mater. Today* 20, 142-154.
- Jiao, Z.B., Luan, J.H., Miller, M.K., Yu, C.Y., Liu, C.T., 2015. Effects of Mn partitioning on nanoscale precipitation and mechanical properties of ferritic steels strengthened by NiAl nanoparticles. *Acta Mater.* 84, 283-291.
- Kadkhodapour, J., Butz, A., Rad, S.Z., 2011a. Mechanisms of void formation during tensile testing in a commercial, dual-phase steel. *Acta Mater.* 59, 2575-2588.
- Kadkhodapour, J., Schmauder, S., Raabe, D., Ziaei-Rad, S., Weber, U., Calcagnotto, M., 2011b. Experimental and numerical study on geometrically necessary dislocations and non-homogeneous mechanical properties of the ferrite phase in dual phase steels. *Acta Mater.* 59, 4387-4394.
- Kapoor, M., Isheim, D., Ghosh, G., Vaynman, S., Fine, M.E., Chung, Y.W., 2014. Aging characteristics and mechanical properties of 1600 MPa body-centered cubic Cu and B2-NiAl precipitation-strengthened ferritic steel. *Acta Mater.* 73, 56-74.

- Kim, D.-K., Kim, E.-Y., Han, J., Woo, W., Choi, S.-H., 2017. Effect of microstructural factors on void formation by ferrite/martensite interface decohesion in DP980 steel under uniaxial tension. *Int. J. Plast.* 94, 3-23.
- Kim, S.-J., Gil Lee, C., Lee, T.-H., Oh, C.-S., 2003. Effect of Cu, Cr and Ni on mechanical properties of 0.15 wt.% C TRIP-aided cold rolled steels. *Scripta Mater.* 48, 539-544.
- Kim, S.H., Kim, H., Kim, N.J., 2015. Brittle intermetallic compound makes ultrastrong low-density steel with large ductility. *Nature* 518, 77-79.
- Lai, Q., Brassart, L., Bouaziz, O., Gouné, M., Verdier, M., Parry, G., Perlade, A., Bréchet, Y., Pardoën, T., 2016. Influence of martensite volume fraction and hardness on the plastic behavior of dual-phase steels: experiments and micromechanical modeling. *Int. J. Plast.* 80, 187-203.
- Li, J., Wang, H., Sun, G., Chen, B., Chen, Y., Pang, B., Zhang, Y., Wang, Y., Zhang, C., Gong, J., Liu, Y., 2015. Neutron diffractometer RSND for residual stress analysis at CAEP. *Nucl. Instrum. Methods A* 783, 76-79.
- Li, Y., Li, W., Liu, W., Wang, X., Hua, X., Liu, H., Jin, X., 2017. The austenite reversion and co-precipitation behavior of an ultra-low carbon medium manganese quenching-partitioning-tempering steel. *Acta Mater.* 146, 126-141.
- Liu, G., Zhang, G.J., Jiang, F., Ding, X.D., Sun, Y.J., Sun, J., Ma, E., 2013. Nanostructured high-strength molybdenum alloys with unprecedented tensile ductility. *Nat. Mater.* 12, 344.
- Matsuno, T., Teodosiu, C., Maeda, D., Uenishi, A., 2015. Mesoscale simulation of the early evolution of ductile fracture in dual-phase steels. *Int. J. Plast.* 74, 17-34.
- Miller, M.K., Nanstad, R.K., Sokolov, M.A., Russell, K.F., 2006. The effects of irradiation, annealing and reirradiation on RPV steels. *J. Nucl. Mater.* 351, 216-222.
- Miller, M.K., Russell, K.F., Thompson, G.B., 2005. Strategies for fabricating atom probe specimens with a dual beam FIB. *Ultramicroscopy* 102, 287-298.
- Petrov, R., Kestens, L., Wasilkowska, A., Houbaert, Y., 2007. Microstructure and texture of a lightly deformed TRIP-assisted steel characterized by means of the EBSD technique. *Mater. Sci. Eng.* 447, 285-297.
- Pierman, A.P., Bouaziz, O., Pardoën, T., Jacques, P.J., Brassart, L., 2014. The influence of microstructure and composition on the plastic behaviour of dual-phase steels. *Acta Mater.* 73, 298-311.

- Raabe, D., Ponge, D., Dmitrieva, O., Sander, B., 2009. Nanoprecipitate-hardened 1.5 GPa steels with unexpected high ductility. *Scripta Mater.* 60, 1141-1144.
- Saleh, M.H., Priestner, R., 2001. Retained austenite in dual-phase silicon steels and its effect on mechanical properties. *J. Mater. Process. Technol.* 113, 587-593.
- Shen, Y.F., Wang, Y.D., Liu, X.P., Sun, X., Peng, R.L., Zhang, S.Y., Zuo, L., Liaw, P.K., 2013. Deformation mechanisms of a 20Mn TWIP steel investigated by in situ neutron diffraction and TEM. *Acta Mater.* 61, 6093-6106.
- Sun, L., Simm, T.H., Martin, T.L., McAdam, S., Galvin, D.R., Perkins, K.M., Bagot, P.A.J., Moody, M.P., Ooi, S.W., Hill, P., Rawson, M.J., Bhadeshia, H.K.D.H., 2018. A novel ultra-high strength maraging steel with balanced ductility and creep resistance achieved by nanoscale β -NiAl and Laves phase precipitates. *Acta Mater.* 149, 285-301.
- Szewczyk, A.F., Gurland, J., 1982. A study of the deformation and fracture of a dual-phase steel. *Metall. Trans. A* 13, 1821-1826.
- Tasan, C.C., Diehl, M., Yan, D., Bechtold, M., Roters, F., Schemmann, L., Zheng, C., Peranio, N., Ponge, D., Koyama, M., Tsuzaki, K., Raabe, D., 2015. An overview of dual-phase steels: advances in microstructure-oriented processing and micromechanically guided design. *Annu. Rev. Mater. Res.* 45, 391-431.
- Torabian, N., Favier, V., Dirrenberger, J., Adamski, F., Ziaei-Rad, S., Ranc, N., 2017. Correlation of the high and very high cycle fatigue response of ferrite based steels with strain rate-temperature conditions. *Acta Mater.* 134, 40-52.
- Wang, C.Y., Shi, J., Cao, W.Q., Dong, H., 2010. Characterization of microstructure obtained by quenching and partitioning process in low alloy martensitic steel. *Mater. Sci. Eng.* 527, 3442-3449.
- Wang, M.M., Tasan, C.C., Ponge, D., Dippel, A.C., Raabe, D., 2015. Nanolaminate transformation-induced plasticity-twinning-induced plasticity steel with dynamic strain partitioning and enhanced damage resistance. *Acta Mater.* 85, 216-228.
- Wang, M.M., Tasan, C.C., Ponge, D., Kostka, A., Raabe, D., 2014. Smaller is less stable: size effects on twinning vs. transformation of reverted austenite in TRIP- maraging steels. *Acta Mater.* 79, 268-281.

- Wang, P., Xiao, N.M., Lu, S.P., Li, D.Z., Li, Y.Y., 2013. Investigation of the mechanical stability of reversed austenite in 13%Cr-4%Ni martensitic stainless steel during the uniaxial tensile test. *Mater. Sci. Eng.* 586, 292-300.
- Wang, X.-L.J.J., 2006. The application of neutron diffraction to engineering problems. *J. Occup. Med.* 58, 52-57.
- Wen, Y.R., Hirata, A., Zhang, Z.W., Fujita, T., Liu, C.T., Jiang, J.H., Chen, M.W., 2013. Microstructure characterization of Cu-rich nanoprecipitates in a Fe-2.5 Cu-1.5 Mn-4.0 Ni-1.0 Al multicomponent ferritic alloy. *Acta Mater.* 61, 2133-2147.
- Weng, K.L., Chen, H.R., Yang, J.R., 2004. The low-temperature aging embrittlement in a 2205 duplex stainless steel. *Mater. Sci. Eng.* 379, 119-132.
- Wu, X., Yang, M., Yuan, F., Wu, G., Wei, Y., Huang, X., Zhu, Y., 2015. Heterogeneous lamella structure unites ultrafine-grain strength with coarse-grain ductility. *P. Natl. Acad. Sci. USA* 112, 14501-14505.
- Xu, S.S., Zhao, Y., Chen, D., Sun, L.W., Chen, L., Tong, X., Liu, C.T., Zhang, Z.W., 2019. Nanoscale precipitation and its influence on strengthening mechanisms in an ultra-high strength low-carbon steel. *Int. J. Plast.* 113, 99-110.
- Xu, S.S., Zhao, Y., Tong, X., Guo, H., Chen, L., Sun, L.W., Peng, M., Chen, M.J., Chen, D., Cui, Y., Sun, G.A., Peng, S.M., Zhang, Z.W., 2017. Independence of work hardening and precipitation strengthening in a nanocluster strengthened steel. *J. Alloys Compd.* 712, 573-578.
- Yan, F.K., Liu, G.Z., Tao, N.R., Lu, K., 2012. Strength and ductility of 316L austenitic stainless steel strengthened by nano-scale twin bundles. *Acta Mater.* 60, 1059-1071.
- Zhang, K., Zhang, M., Guo, Z., Chen, N., Rong, Y., 2011. A new effect of retained austenite on ductility enhancement in high-strength quenching-partitioning- tempering martensitic steel. *Mater. Sci. Eng.* 528, 8486-8491.
- Zhang, M., Li, L., Fu, R.Y., Krizan, D., De Cooman, B.C., 2006. Continuous cooling transformation diagrams and properties of micro-alloyed TRIP steels. *Mater. Sci. Eng.* 438-440, 296-299.
- Zhang, M.D., Hu, J., Cao, W.Q., Dong, H., 2014. Microstructure and mechanical properties of high strength and high toughness micro-laminated dual phase steels. *Mater. Sci. Eng.* 618, 168-175.

Zhao, J.-l., Xi, Y., Shi, W., Li, L., 2012. Microstructure and mechanical properties of high manganese TRIP steel. *J. Iron Steel Res. Int.* 19, 57-62.

Figure captions

Fig. 1. Schematic of the sample dimensions and position for the measurements of lattice strain distributions during in-situ tensile loading on the neutron diffractometer.

Fig. 2. Mechanical properties of the solid-solution (SS) treated steel and aged steel (AG0.5h) at 500 °C for 0.5 h. (a) Engineering stress-strain curves of the SS and AG0.5h steel. (b) Tensile properties of our FS dual-phase steel compared with those of other high-performance materials.

Fig. 3. Microstructures of the solid-solution (SS) treated steel and the aged steel (AG0.5h) at 500 °C for 0.5 h. EBSD phase maps of (a) the SS and (b) AG0.5h steels, showing the skeleton construction in the two steels. Orientation mappings with low and high angle grain boundaries for (c) the SS and (d) AG0.5h steels. RD, rolling direction; ND, normal direction; TD, transverse direction.

Fig. 4. Grain size distributions of (a) BCC martensite phase and (b) FCC austenite phase in SS steel, (c) BCC martensite phase and (d) FCC austenite phase in AG0.5h steel.

Fig. 5. Selected X-ray Diffraction (XRD) spectra for both of the steels before (SS and AG0.5h) and after the tensile tests (SS-AT and AG0.5h-AT). The austenite content confirms the occurrence of transformation-induced plasticity (TRIP) in both steels.

Fig. 6. Hardening response and elemental distribution in the two phases determined by atom probe tomography (APT). (a) Hardness as a function of aging time at 500 °C for martensite and austenite. 3D APT atom maps of the distribution of the Cu, Ni, Al and Mn solute elements in austenite (b) and martensite (c) of AG0.5h steel. Proximity histograms of carbide (d), Cu (e) and NiAl (f)

nanoprecipitates, confirming age hardening of the martensite induced by high-density Cu and NiAl precipitates.

Fig. 7. Deformation mechanism and true stress-strain curve with the strain hardening rate of the dual-phase steel prior to aging (SS steel). (a) Response of lattice strains to the applied stress along the tensile direction. (b) True stress-strain curve with the strain hardening rate for the SS steel, showing a continuous decrease in the uniform deformation.

Fig. 8. Deformation mechanism of the AG0.5h dual-phase steel with precipitate-strengthened martensite. (a) Response of lattice strains to the applied stress along the tensile direction for AG0.5h steel, three deform stages (elastic deformation I, early II and late III uniform deformation) are marked. Normalized diffraction intensity (b) and evolution of full-width half-maximum (FWHM) (c) as a function of applied stress for the AG0.5h steel. True stress-strain curve with the strain hardening rate (d) and Kernel average misorientation (KAM) map (e) of the austenite in the AG0.5h steel after tensile deformation.

Fig. 9. Inverse pole figures of the AG0.5h steel with respect to the tensile axis (TA) for martensite and austenite before and after the tensile test. $\{110\}$ //TA in martensite and $\{100\}$ //TA in austenite indicate the progressive alignment of the slip systems between the martensite and austenite.

Fig. 10. APT atom map along with the one-dimensional concentration profiles of a duplex precipitate in AG0.5h steel. The nanoscale precipitate consists of a Cu-rich precipitate (enriched mainly with Cu and Ni) and a NiAl rich precipitate (enriched with Ni, Al and Mn), forming a coprecipitated particle.

Fig. 11. TEM micrographs of AG0.5h steel after uniform deformation with selected area diffraction image. The phase boundaries with the favorable K-S orientation relationship between the martensite and the soft austenite are beneficial for the deformation transfers from martensite to austenite and the accommodation of the dislocations (indicated by red arrows) moving out from the hard martensite, suppressing stress localization and retarding crack initiation. (For interpretation of the references to color in this figure legend, the reader is referred to the Web version of this article.)

Fig. 2

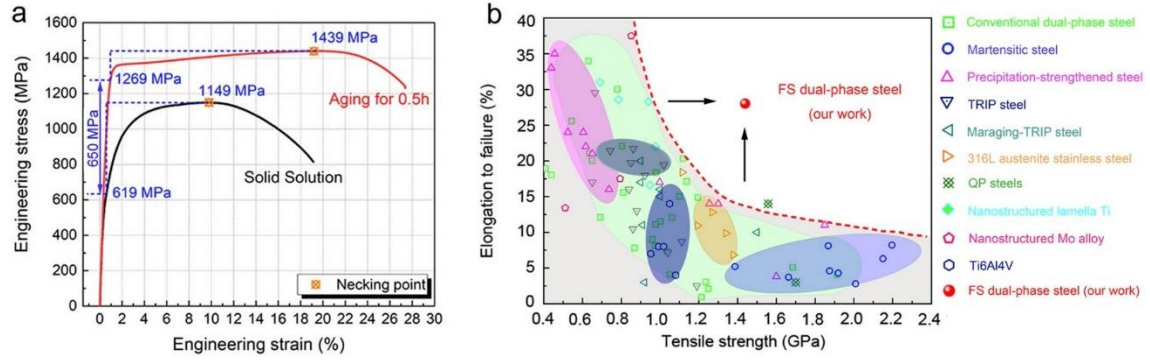


Fig. 3

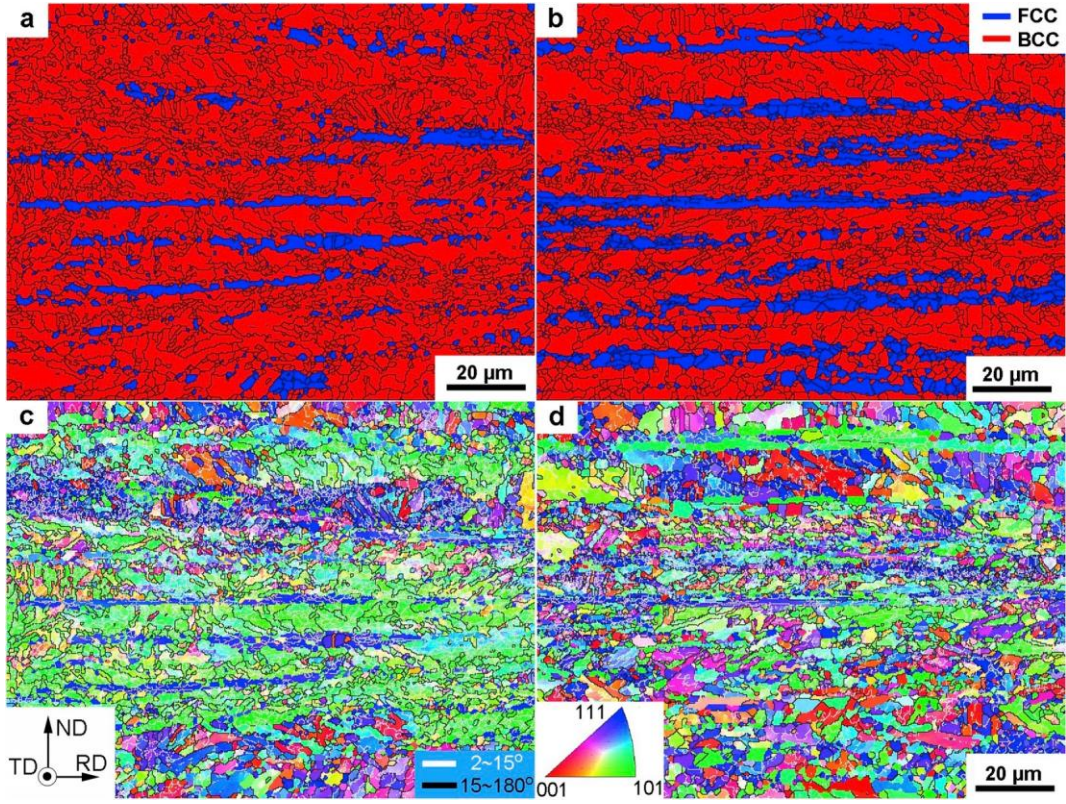


Fig. 4

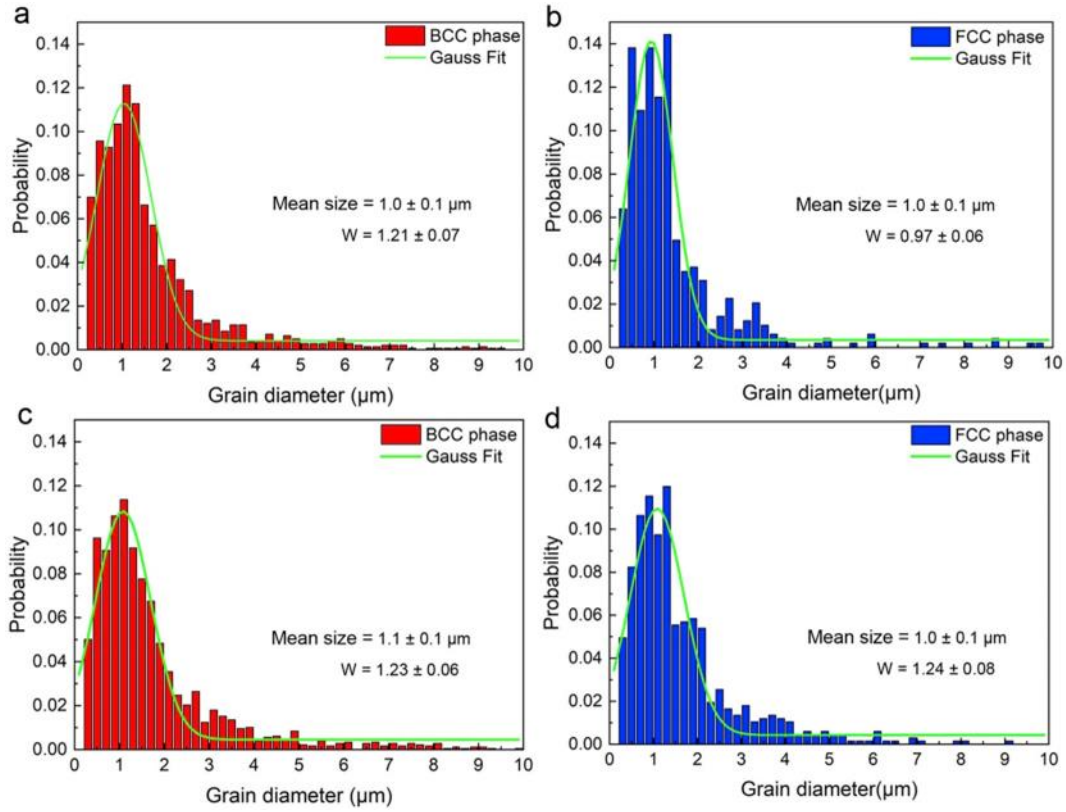


Fig. 5

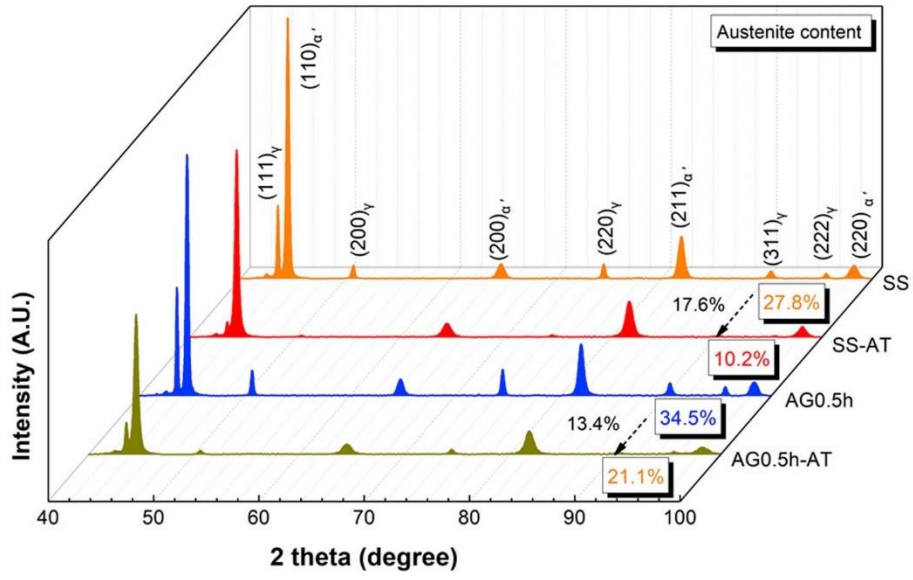


Fig. 6

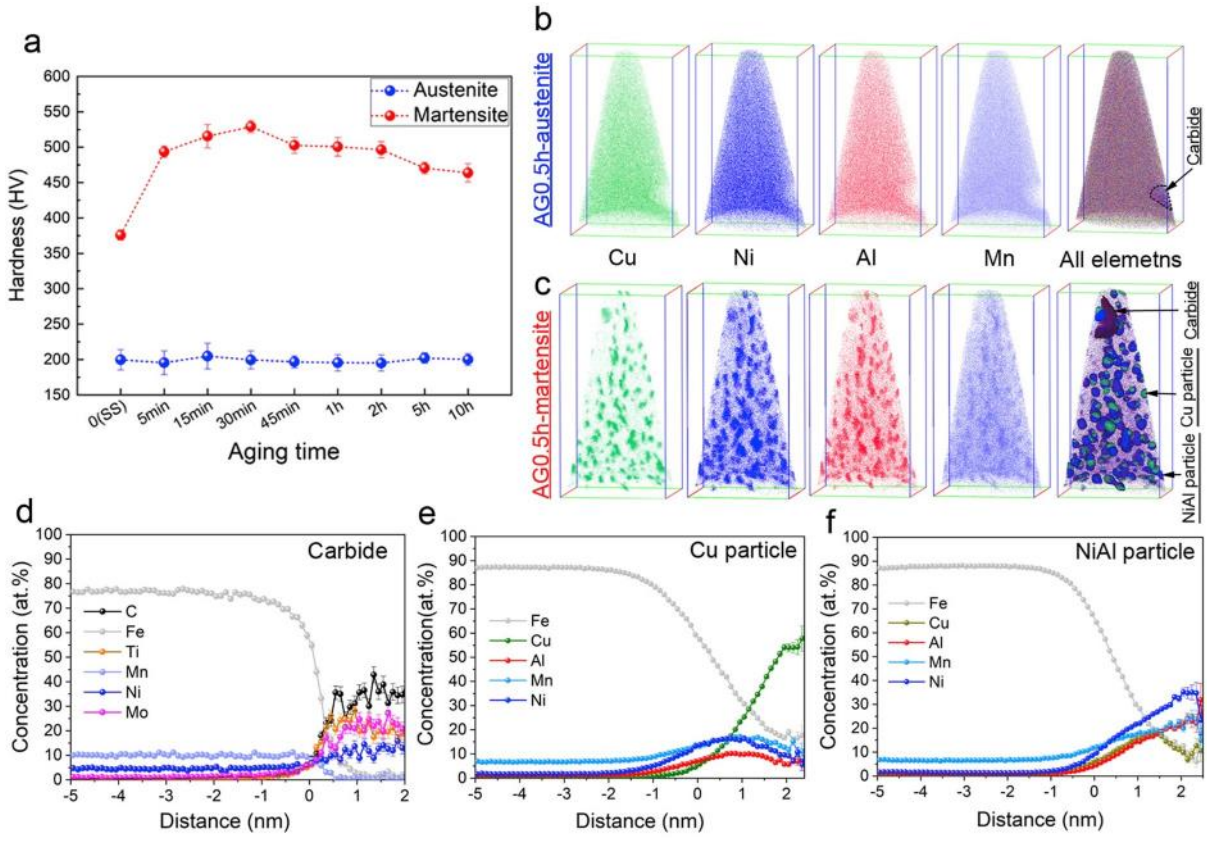


Fig. 7

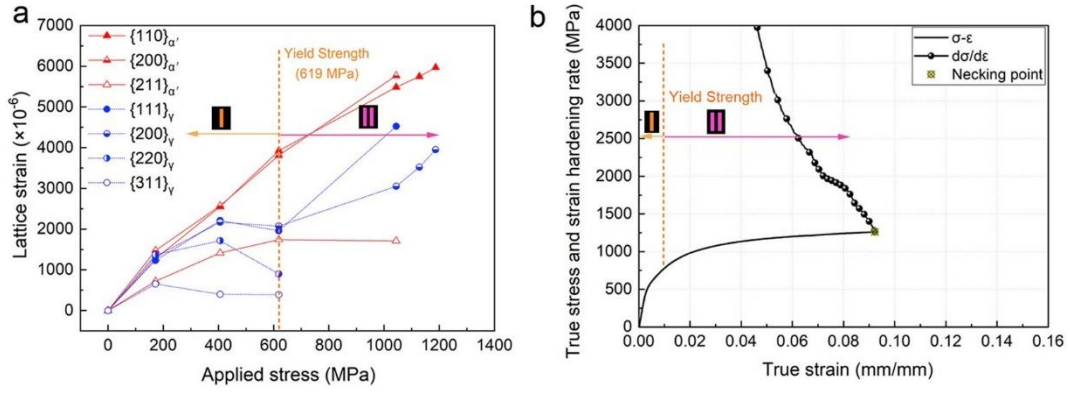


Fig. 8

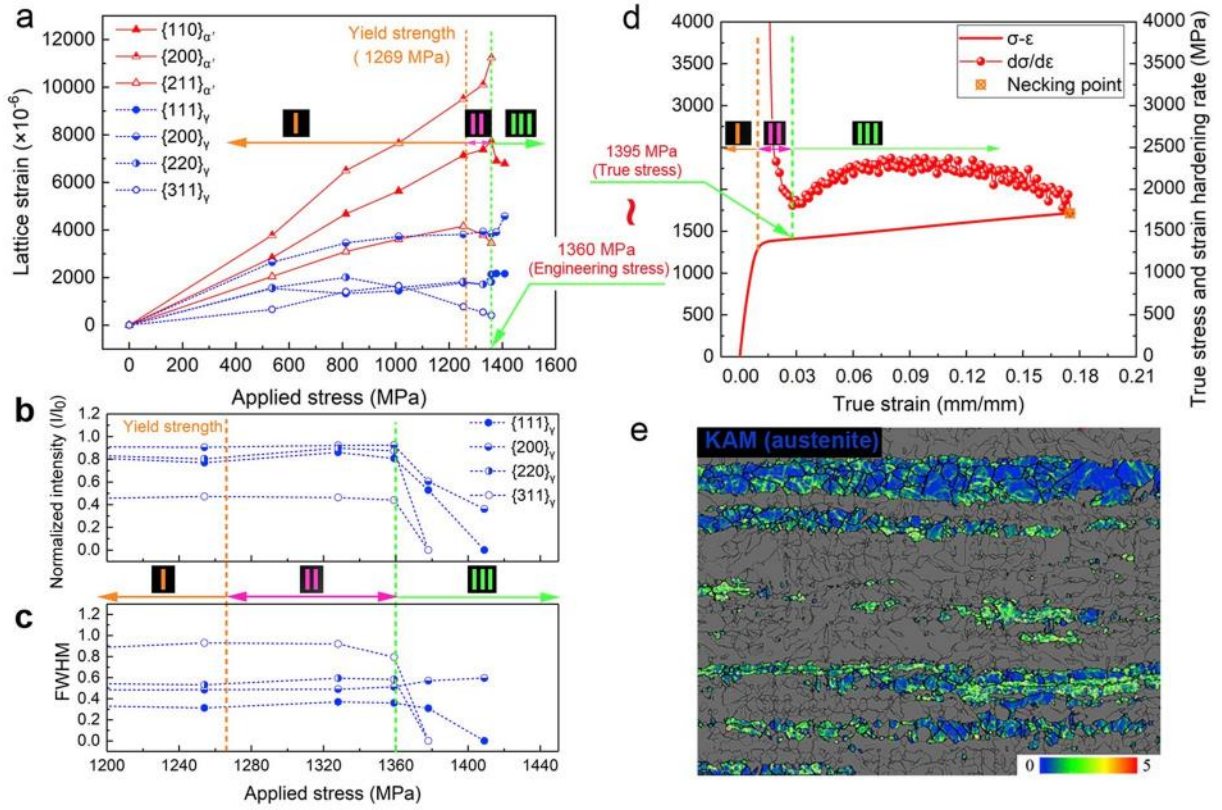


Fig. 9

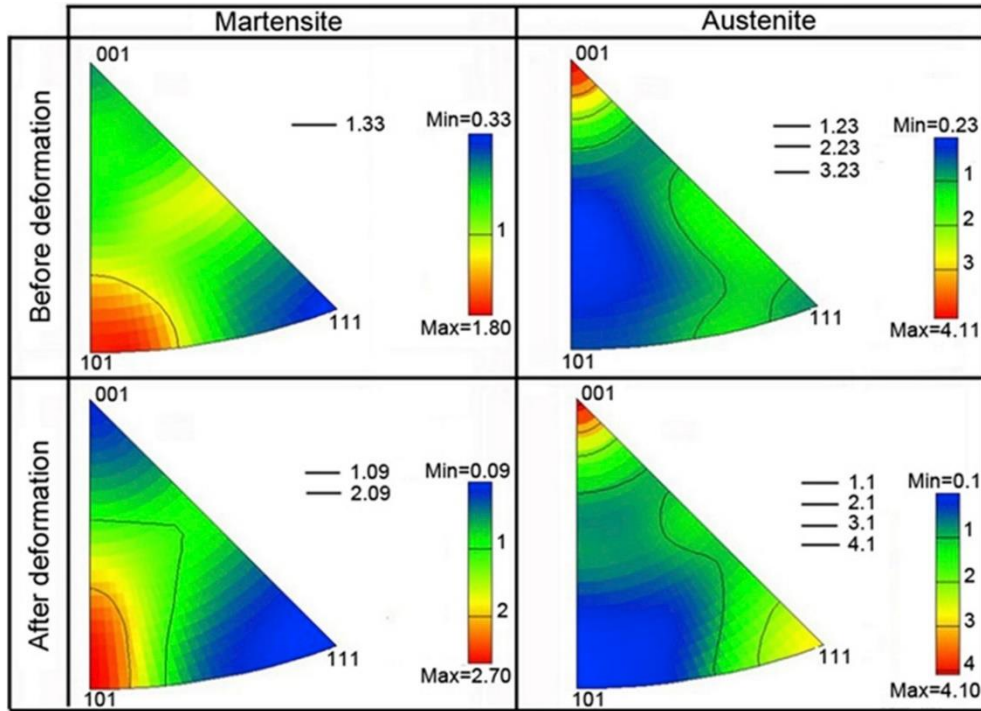


Fig. 10

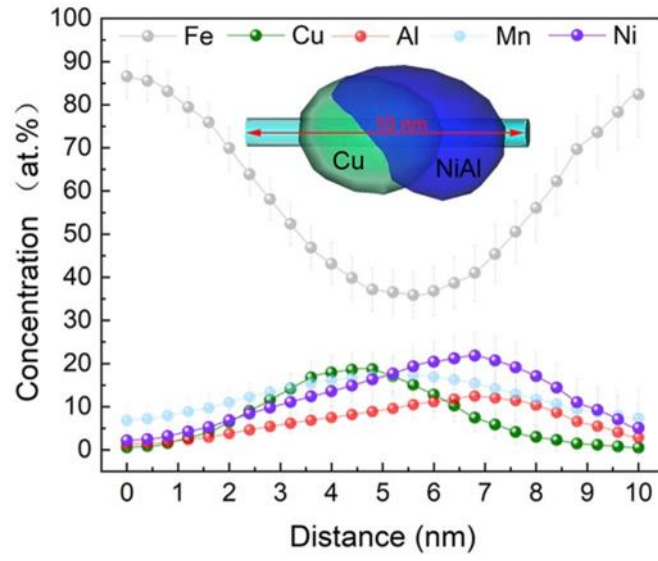


Fig. 11

